Evolution of Crystallographic Texture during Equal Channel Angular Extrusion of Copper: The Role of Material Variables

SATYAM SUWAS, ROXANE ARRUFFAT-MASSION, LÁSZLÓ S. TÓTH, JEAN-JACQUES FUNDENBERGER, ANDRÉ EBERHARDT, and WERNER SKROTZKI

The evolution of crystallographic texture during equal channel angular extrusion (ECAE) using route A has been investigated experimentally as well as by simulations for three types of materials: pure, commercially pure, and impure (cast) copper. The ECAE texture of copper can be compared with simple shear textures. However, there are deviations in terms of location of the respective components. These differences can be nearly reproduced using a recent flow line approach for ECAE deformation (L.S. Tóth, R. Arruffat-Massion, L. Germain, S.C. Baik, and S. Suwas: *Acta Mater.*, 2004, vol. 52, pp. 1885-98) with the help of the viscoplastic self-consistent polycrystal model. The main texture components common to all three materials are A_{1E} and $B_E/\overline{B}_E$; the latter ones are significantly stronger in the cast material. The effect of further deformation on texture modification depends on material variables, such as purity, initial microstructure, and texture.

I. INTRODUCTION

EQUAL channel angular extrusion (ECAE) is being viewed as one of the potential deformation processing techniques for grain refinement to submicron size or sometimes up to nanometer size of bulk materials. The process is also associated with the development of specific crystallographic textures, which add to the mechanical characteristics of the as-processed materials. In ECAE, a billet of circular or square cross section is deformed in a narrow deformation zone at the plane of intersection of two die channels of the same cross section and the strain mode approximates closely to simple shear.[1–4] As the overall billet geometry remains nearly constant during ECAE, multiple passes through the die are possible without any reduction in cross-sectional area. This allows materials to be deformed to very high plastic strains ($\bar{\varepsilon}_{von\ Mises} \sim 1.15$ per pass) that cannot be readily obtained in more conventional processes, such as rolling.

Texture development in this deformation process has not been paid enough attention as compared to the microstructural aspects. However, it has been speculated[5] that the texture developed and its relationship with the shear plane are the key factors that affect grain refinement in subsequent stages. Some recent literature that deals with texture formation during ECAE are very specific regarding the initial conditions of the materials investigated. Most of the works deal with texture formation in Al and Al alloys[6–9] as well as in Cu,[10–18] and a few on other fcc materials such as Ni,[19] and very recently on Ag.[20] A few articles have been published on texture evolution in Fe[21,22] during ECAE.

In the present work, an attempt has been made to understand texture development in copper during route A of ECAE deformation, as a function of the initial texture of different starting materials. The choice of materials has been done in such a way that different types of chemical compositions and microstructural conditions, which are generally used as the starting materials during processing for different industrial applications, are studied. The metallurgical variables that have been considered in this study are (1) purity, (2) grain size, and (3) microstructural heterogeneity (due to the presence of a second phase formed by impurities in one of the materials). Although in such situations it is difficult to clearly isolate the individual effects of each of the preceding variables on texture evolution, it appears worth examining these conditions in order to know the limits. The texture analysis has been carried out using the method of the orientation distribution function (ODF) in order to have a complete description of texture development. Further, the textures have been simulated using the techniques previously proposed by the authors. The experimental and simulation results have been discussed in light of simulations using other similar methods involving shear deformation and the existing relevant models.

II. MATERIALS AND EXPERIMENTAL PROCEDURE

A. *Materials and ECAE Experiments*

Three types of copper, one with 99.99 pct purity (hereafter referred to as material I) obtained in extruded and annealed form, a second one with 99.89 pct purity (hereafter referred to as material II) also extruded + annealed, and a third one with 99.56 pct purity (hereafter referred to as material III) as cast + homogenization annealed, were used for the current study. Specimens with 10×10 mm square cross section and 100 mm length were machined from these annealed bars. The ECAE experiments were carried out at a crosshead speed of 1 mm s^{-1} at room temperature using a

SATYAM SUWAS, formerly Postdoctor, Laboratory of Physics and Mechanics of Materials, Université de Metz, is Assistant Professor, Department of Metallurgy, Indian Institute of Science, Bangalore, India. ROXANE ARRUFFAT-MASSION, Postdoctor, and LÁSZLÓ S. TÓTH and ANDRÉ EBERHARDT, Professors, Laboratory of Physics and Mechanics of Materials, and JEAN-JACQUES FUNDENBERGER, Professor, Laboratory of Texture Studies and Applications to Materials, are with the Université de Metz, Ile du Saulcy, F-57045 Metz, Cedex 01, France. Contact e-mail: toth@univ-metz.fr WERNER SKROTZKI, Professor, is with the Institute for Structural Physics, Technical University of Dresden, 01062 Dresden, Germany.

Manuscript submitted February 23, 2005.

Zwick (Ulm, Germany) 200 kN screw driven machine and a die set with rectangular intersection of the extrusion channels without any rounding of the corner region. There were no sliding surfaces of the die to reduce friction. Molybdenum sulfite was used for lubrication of the contact surfaces. The dimension of horizontal (outlet) channel of the die was modified such that it takes care of possible spring back in order to make the reinsertion of the sample in the vertical channel. This was done in the following way. The first 25-mm length of the horizontal channel (the portion joining the vertical channel) had the cross section (9.9×9.9) mm^2, while the rest, 15-mm length of the horizontal channel, had the area of cross section (10.5×10.5) mm^2. The specimens were extruded in route A, *i.e.*, without rotation around their longitudinal axis between passes. The number of ECAE passes was limited to three. Microstructures of the starting materials as well as some of the deformed materials were examined using a Leo scanning electron microscope (SEM). A few deformed materials were also examined under a transmission electron microscope (TEM), JEOL* 2000 FX, operated at 200 kV.

*JEOL is a trademark of Japan Electron Optics Ltd., Tokyo.

B. *Measurement and Representation of Texture*

Texture measurements were carried out by X-ray diffraction using a Siemens D-5000 Texture Goniometer (Cu K_α radiation, $\lambda = 1.5406$ Å). The (111), (200), and (220) pole figures were recorded on the midhorizontal plane (*XZ*) of the sample (Figure 1) parallel to the direction of extrusion using Schultz-reflection mode (illuminated area was 25×10 mm). For each sample, texture was examined by plotting pole figures as well as by calculating ODFs. The ODFs are more precise as they describe the crystallite orientation densities in a three-dimensional orientation space defined by the Euler angles ϕ_1, ϕ, and ϕ_2. The ODFs were calculated and plotted using the software developed at LETAM and by Van Houtte[23] following the series expansion method of Bunge[24] with a limit of expansion rank $l_{max} = 32$. Triclinic sample symmetry was imposed in the calculation of the ODF because the only sample symmetry that may exist in the ODF of an ECAE-deformed sample is a mirror symmetry with respect to the ND-ED plane. This symmetry, however, is only preserved if it existed already before testing. Symmetries are discussed further in Section III.

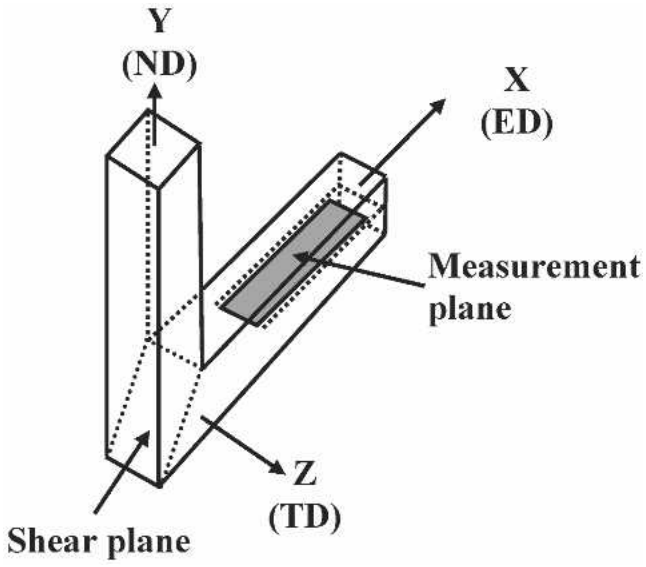

Fig. 1—The geometry of ECAE deformation and measurement plane.

III. EXPERIMENTAL RESULTS AND ANALYSIS

Figure 2 shows SEM micrographs of the materials before ECAE. As can be seen, the microstructure of material I consists of recrystallized, almost equiaxed grains with a grain size in the range of 10 to 40 μm, while material II shows a similar grain shape but with larger grain size: 100 to 200 μm. The microstructure of material III displays typical coarse grain structure (Figure 2(c)). The pores apparent in the microstructure, which are formed due to removal of inclusion particles during polishing, clearly depict the grain boundaries in this material. The grain size in this material is very large, about 1 to 3 mm.

The (111) pole figures of the starting materials are shown in Figure 3 in the laboratory reference system projected onto the ND plane, which is initially parallel to the sample longitudinal axis. The textures of the three starting materials are very different. Material I (Figure 3(a)) shows somewhat weak texture of a wrought + annealed material comprised of <100> and <110> fibers, while the texture of material II (Figure 3(b)) shows a strong <100> fiber together with a weak <111>. In the case of material III, a spotty pole figure is recorded (Figure 3(c)), which is characteristic of very coarse-grained structures with differently oriented grains. The textures of materials I and III have also been measured using neutron diffraction, and similar results were obtained (not shown here).

Before we proceed in the analysis of the deformation textures after ECAE passes, it is necessary to highlight the relation between ECAE textures and textures of simple shear. Now it is commonly accepted that the ideal orientations of ECAE textures are the same as those of simple shear with the shear plane being the 45 deg plane of the die; they were identified in Reference 16 in the ECAE reference system. Simple shear textures are characterized by two partial fibers:[25] (1) {111} $\|$ shear plane, containing $A/\overline{A}$ and A_1*, A_2* ("A" fiber); and (2) <110> $\|$ shear direction, having the $A/\overline{A}$, $B/\overline{B}$, and C as the main ideal components ("B" fiber). As the shear plane is coincident with the 45 deg plane of the die (Figure 1), the corresponding components for ECAE textures are obtained by expressing the simple shear ideal orientations in the *X-Y-Z* reference system. This operation implies a rotation of 45 deg around the TD axis. The so-obtained components are the ideal components of the ECAE process and are distinguished from the ideal shear components by a suffix "E" in Table I.[16] In order to ease the reading of the pole figures measured on the *XZ* plane, a key figure has been constructed containing the ideal components as they appear in a {111} pole figure on the ED-TD plane (Figure 4). The consequence of the possible mirror

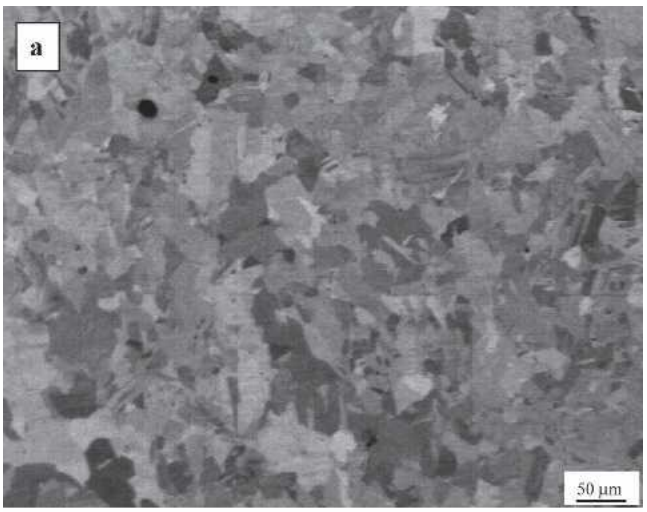

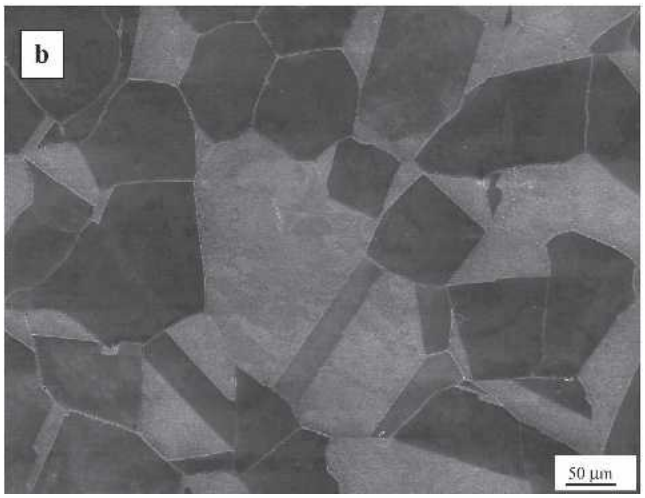

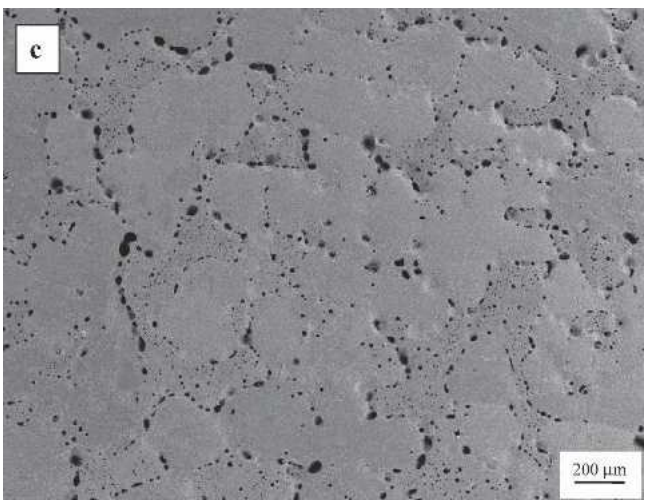

Fig. 2—Low-magnification SEM micrographs of the materials before ECAE: (*a*) material I, (*b*) material II, and (*c*) material III.

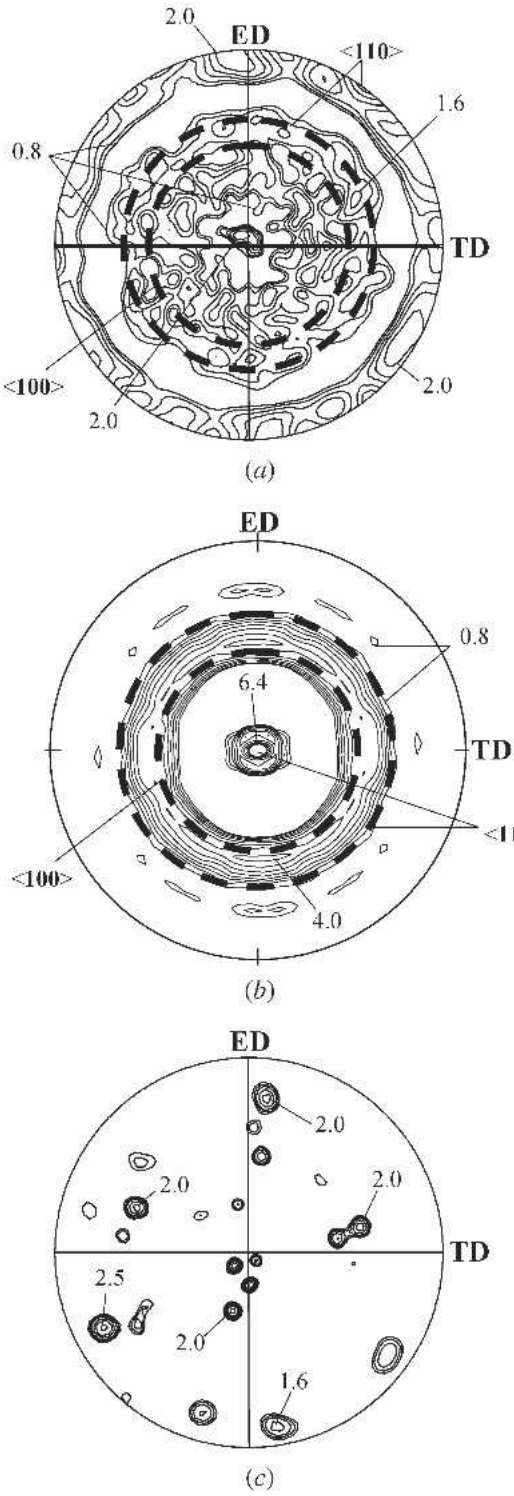

Fig. 3—(111) pole figures of the starting materials: (*a*) material I, (*b*) material II, and (*c*) material III. The main intensity locations are labeled and the ideal fibers are indicated. Iso-values for all pole figures: 0.8, 1.0, 1.3, 1.6, 2.0, 2.5, 3.2, 4.0, 5.0, 6.4.

symmetry with respect to the ED-ND plane is that the A_E and B_E components must have the same intensities as the $\overline{A}_E$ and $\overline{B}_E$ components, respectively (Figure 4). The A_{1E} and A_{2E} components are each self-symmetric; therefore, their intensities can be different. Although the simple shear nature of the deformation process should lead to a monoclinic symmetry of the textures with respect to the TD axis, this symmetry is not necessarily valid because the strain mode is not

Table I. The Ideal Orientations of Fcc ECAE Textures

	Miller Indexes			Euler Angles		
	ED	ND	TD	ϕ_1	ϕ	ϕ_2
A_{2E}	[25 $\bar{3}$ 3]	[6 25 $\bar{25}$]	[011]	9.74	45	0
	[$\bar{3}$ 3 25]	[25 $\bar{25}$ 6]	[110]	99.74	90	45
A_{1E}	[6 $\bar{25}$ 25]	[25 3 $\bar{3}$]	[011]	80.37	45	0
	[$\bar{25}$ 25 6]	[3 $\bar{3}$ 25]	[110]	170.37	90	45
C_E	[$\bar{1}\bar{0}\bar{0}$ $\bar{7}\bar{1}$ 71]	[100 $\bar{7}\bar{1}$ 71]	[011]	135	45	0
	[71 $\bar{7}\bar{1}$ 100]	[71 $\bar{7}\bar{1}$ $\bar{1}\bar{0}\bar{0}$]	[110]	45	90	45
A_E	[2 $\bar{2}\bar{0}$ 9]	[20 $\bar{2}$ $\bar{9}$]	[112]	45	35.26	45
$\bar{A}_E$	[$\bar{2}$ 20 $\bar{9}$]	[$\bar{2}\bar{0}$ 2 9]	[112]	225	35.26	45
B_E	[27 $\bar{1}\bar{0}\bar{0}$ 73]	[100 $\bar{2}\bar{7}$ $\bar{7}\bar{3}$]	[111]	45	54.74	45
	[$\bar{1}\bar{0}\bar{0}$ 73 27]	[$\bar{2}\bar{7}$ $\bar{7}\bar{3}$ 100]	[111]	165	54.74	45
$\bar{B}_E$	[$\bar{7}\bar{3}$ $\bar{2}\bar{7}$ 100]	[73 $\bar{1}\bar{0}\bar{0}$ 27]	[111]	105	54.74	45
	[$\bar{2}\bar{7}$ 100 $\bar{7}\bar{3}$]	[$\bar{1}\bar{0}\bar{0}$ 27 73]	[111]	225	54.74	45

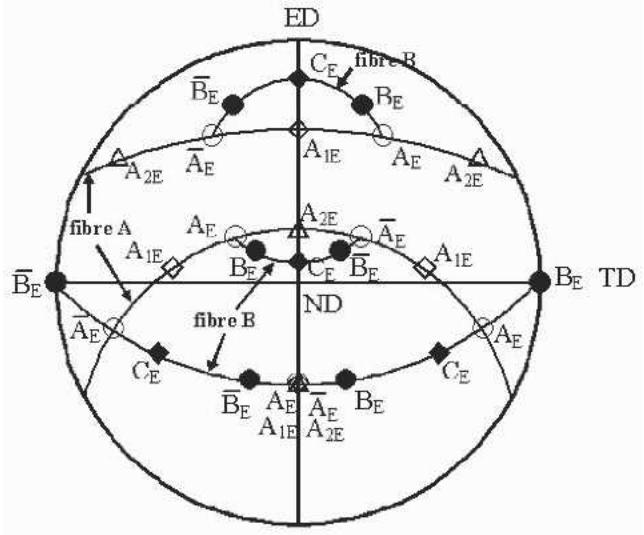

Fig. 4—A key figure representing the location of standard ECAE components in the ED-TD projection plane.

exactly simple shear in the die. Experimental[8] and theoretical flow line analyses[16] as well as finite-element simulations[18] show that there are differences from simple shear. Even if monoclinic symmetry can be valid with a certain approximation in route A textures, this symmetry is definitely lost when the sample is subjected to route B strain path.

The changes in texture are quite apparent after ECAE deformation (Figure 5). Strong texture develops after even one pass, it continues to strengthen up to the second pass, and then it weakens a little. This trend is the same for all three materials. The pole figures appear nearly symmetrical about the ND-ED plane for materials I and II, while the symmetry is significantly less for material III. Some tilts of the pole figures around the ND axis are visible in the second and third passes of materials I and II, probably due to some misalignment of the samples. Significant differences can be seen between the textures of all three materials.

A detailed analysis of the textures has been carried out using the ODF representation. The advantage of displaying the ECAE textures in orientation space in contrast to pole figures is that the ideal orientations appear separately, without overlapping. Figures 6(a) through (c) represent the $\phi_2 = 0$ deg and $\phi_2 = 45$ deg sections of the ODFs, which are sufficient if one is interested only in the ideal components of the textures. The ideal ECAE texture components are presented in a key ODF figure. The examination of the ODFs reveals that the maximum intensities $f(g)_{max}$ increase with the progress of deformation up to two passes in materials I and III; thereafter, they decrease substantially (Table II). In material II, $f(g)_{max}$ decreases continuously.

The ideal components do not necessarily appear in their ideal positions as they are defined in Table I. There are shifts from the ideal locations, which can be relatively high; refer to their values in Tables III through V. Such tilts of the ideal components were also examined in Reference 17; they concern mostly shifts in the ϕ_1 direction of the ODF space meaning a rotation around the TD axis. Although some misalignment by a few degrees might have occurred in the texture measurement, they may affect rotations around the ND axis (as discussed above) and not the TD axis.

In material I, the shifts are relatively low in the first pass; however, for passes 2 and 3, the shift increases dramatically and becomes positive for each component (Table III). The $\phi_2 = 0$ deg section of the ODF of one-pass ECAE-processed material I shows a weak and spread A_{2E} and strong C_E and A_{1E} components (Figure 6(a) and Table III). The $\phi_2 = 45$ deg section displays a continuous orientation distribution in the ODF joining the A_E, B_E, and C_E components, which is the B fiber in simple shear. The fiber between B_E and A_{1E} is probably just an appearance because of the strong intensity of the A_{1E} component. After the second pass, all texture components are significantly rotated from their respective ideal positions, as can be seen in both the $\phi_2 = 0$ and 45 deg sections and in Table III. The B fiber shrinks to its B_E component only. Consequent to the simultaneous strengthening of the B_E and A_{1E} components, the continuous spread between these components looks like a fiber. The trend is maintained in the three-pass ECAE-deformed material, too. The texture appears to be somewhat stable, with little decrement in intensity.

The course of texture evolution in material II appears to be somewhat similar to material I, however, with subtle differences (Figure 6(b)). In the one-pass deformed material, C_E is the strongest component as in the case of material I, while the A_{1E} component is substantially weaker, which is in contrast to material I. The A_{2E} component, which was weak in material I, is practically nonexistent in material II. Another difference is the existence of a rotated cube component, which is retained from the initial texture. More deformation passes, however, bring some similarities in the textures. In the texture of two-pass deformed material II, the strongest component is A_{1E}, and C_E almost disappears. The $B_E/\bar{B}_E$ components strengthens. After three passes, as in material I, weakening of A_{1E}, vanishing of C_E, and further strengthening of $B_E/\bar{B}_E$ are observed. The only contrasting feature from the three-pass deformed material I is the strengthening of the A_{2E} component in material II. The shifts from respective ideal locations are generally less than those observed in material I (Table IV).

In material III, all of the aforementioned components are seen after the first pass with varying shifts (Figure 5(c) and

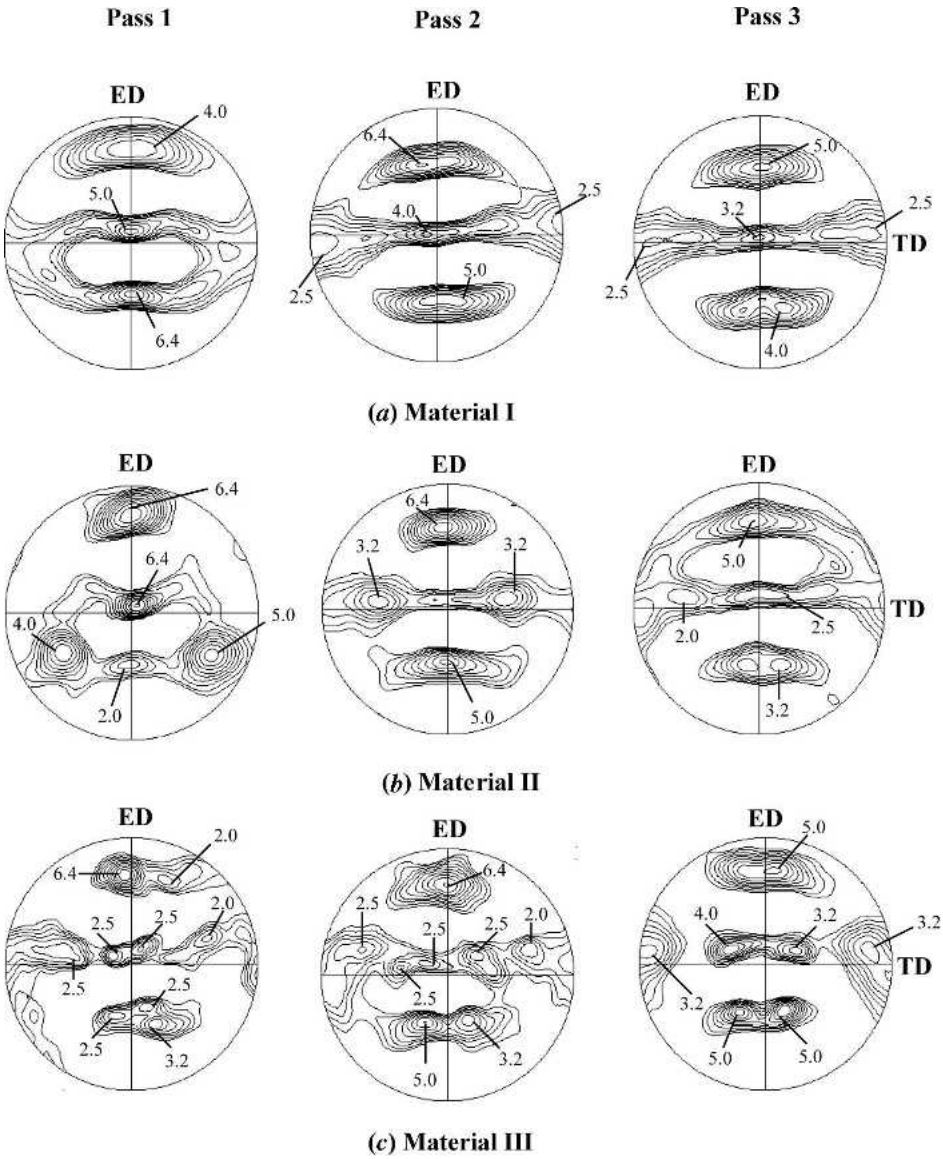

Fig. 5—(111) pole figures of the one-, two-, and three-pass ECAE-deformed materials: (*a*) material I, (*b*) material II, and (*c*) material III. Numbers indicate the intensities of the local maximum contour lines. Iso-values for all pole figures: 0.8, 1.0, 1.3, 1.6, 2.0, 2.5, 3.2, 4.0, 5.0, 6.4.

Table V). Some additional ones also appear in the ODF. A particularity of the textures is the *nonequal* intensities of the $B_E/\overline{B}_E$ and $A/\overline{A}$ components. Actually, these ideal positions are not self-symmetric (see also above); therefore, they do not have to display equal intensities when there is no symmetry in the test or in the sample. The trend in the variation of the strength is also somewhat different. In this case, the one-pass deformed material shows the A_{1E} component as the strongest, like material I, followed by the $B_E/\overline{B}_E$, and C_E components. The A_{1E} component, however, weakens with further ECAE passes (unlike materials I and II), while the $B_E/\overline{B}_E$ components generally strengthen. Their associated shifts from respective ideal positions vary with the number of passes (Table V). In conclusion, the texture of material III is distinct from the other two materials mostly in terms of the weak intensities of the A_{1E} and A_{2E} components and the high intensity of the $B_E/\overline{B}_E$ components in the second and third passes.

IV. TEXTURE SIMULATIONS

A. *Modeling Parameters*

The details of simulation procedures, which were employed in this work, are published in Reference 17. For the Reader's convenience, they are briefly described here. First, the initial textures of the three materials (shown in Figure 3) were discretized to 3000 grain orientations. They were then introduced into the Taylor viscoplastic full constraints (FC) or self-consistent (SC) polycrystal models. The strain rate sensitivity index m of crystallographic slip was chosen to be 0.05 because m values lower than 0.05 led to very nearly the same texture results. Also, the convergency of the numerical procedure was better for $m = 0.05$. For the SC simulations, the finite-element tuned SC model was employed in its isotropic version (isotropic in the sense of the interaction between the homogeneous equivalent medium and a grain[26]). The 12 {111} <110> slip systems of an fcc crystal were

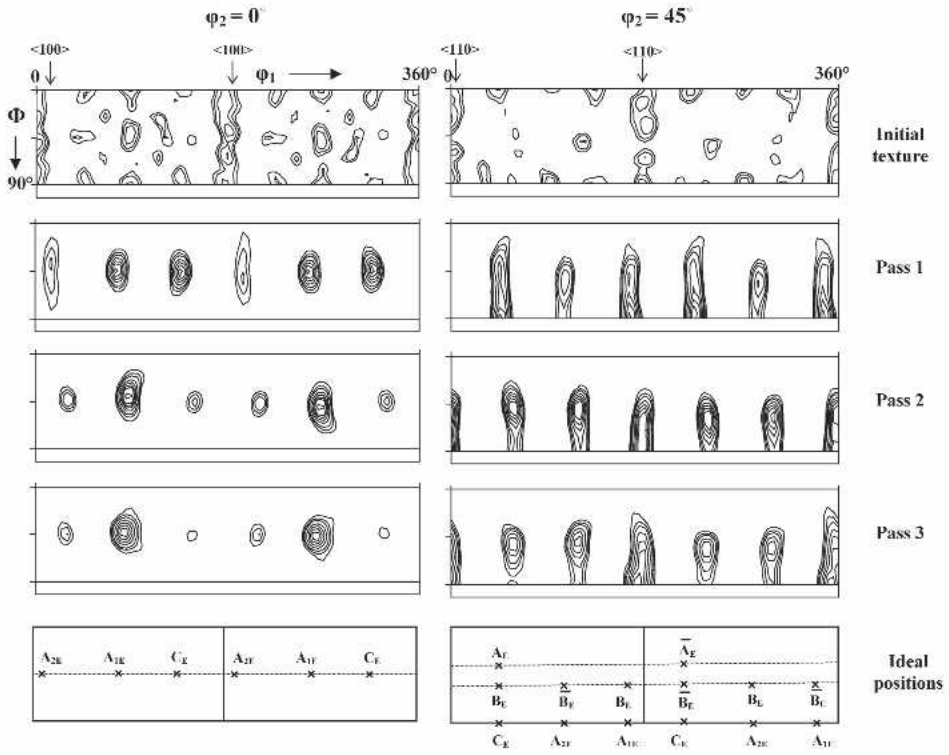

(*a*)

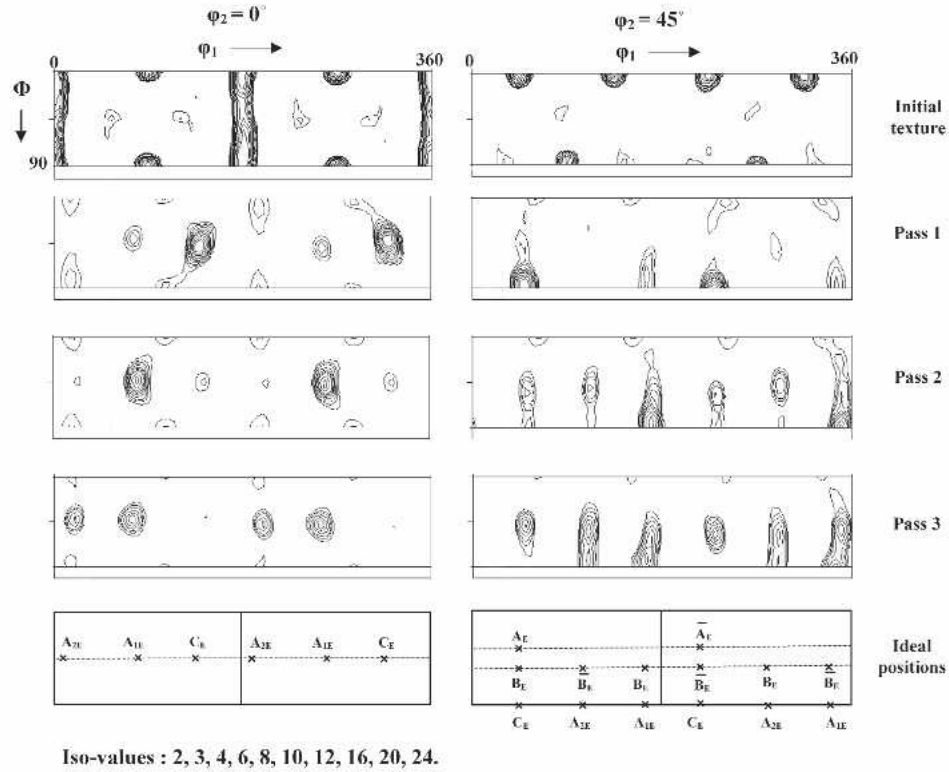

(*b*)

Fig. 6—ϕ_2 = 0 deg and ϕ_2 = 45 deg sections of the experimental ODF for the three ECAE-processed samples of (*a*) material I, (*b*) material II, and (*c*) material III (a key figure representing the location of standard ECAE components is also given along with each of these figures).

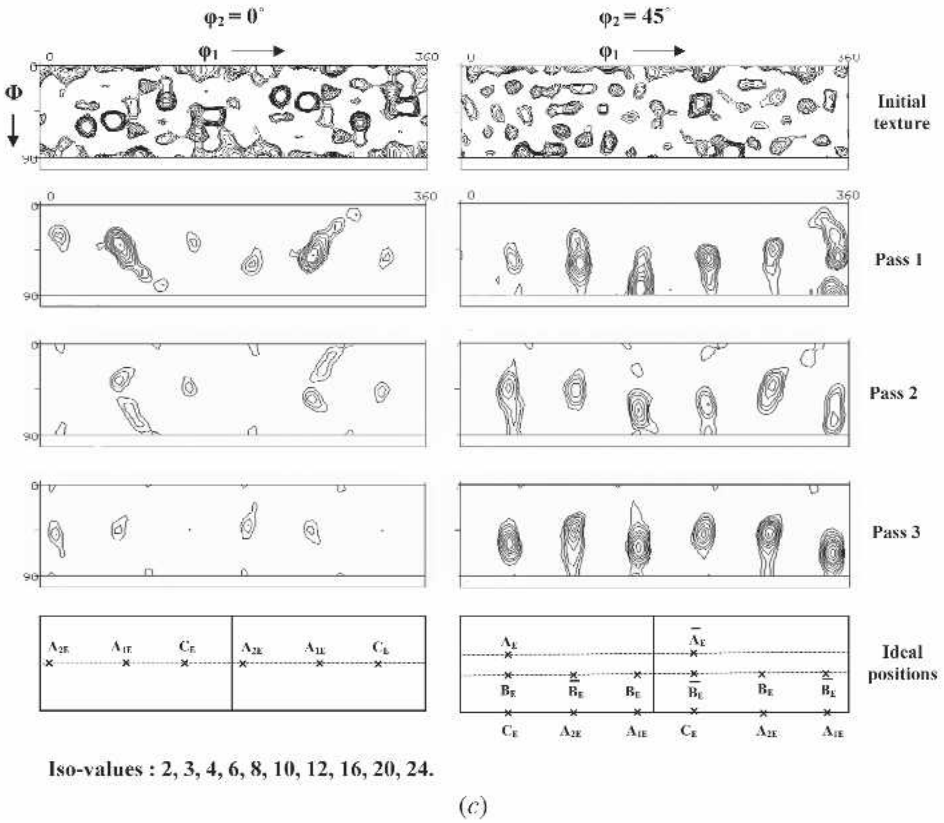

(*c*)

Fig. 6—(Continued). $\phi_2 = 0$ deg and $\phi_2 = 45$ deg sections of the experimental ODF for the three ECAE-processed samples of (*a*) material I, (*b*) material II, and (*c*) material III (a key figure representing the location of standard ECAE components is also given along with each of these figures).

Table II. Values of the Measured ODF Peak Intensities $f(g)_{max}$ and Texture Strength T

Sample	Pass	$f(g)_{max}$	Texture Strength T
Material I	0	6.81	2.88
	1	13.85	5.89
	2	18.99	7.62
	3	13.68	4.80
Material II	0	37.40	11.02
	1	33.98	6.27
	2	23.15	5.03
	3	12.99	4.03
Material III	0	92.35	101.28
	1	27.06	5.58
	2	40.39	3.86
	3	36.33	5.81

employed with self- and latent hardening.[17] It should be noted that the effect of hardening on the evolution of texture was found to be very small.

Two models were considered for the deformation mode within the ECAE die: (1) the so-called discontinuous shear model, originally proposed by Segal,[1] in which the deformation is simple shear that takes place on the 45 deg intersection plane of the two channels; and (2) the newly introduced flow line model that uses rounded flow lines with the help of an analytical flow function.[17]

For the discontinuous shear model, the velocity gradient is constant and given by (in the *X-Y-Z* reference system fixed to the die (Figure 1))

$$L = \frac{\dot{\gamma}}{2}\begin{pmatrix} 1 & -1 & 0 \\ 1 & -1 & 0 \\ 0 & 0 & 0 \end{pmatrix} \qquad [1]$$

Here, $\dot{\gamma}$ is the rate of shear on the 45 deg plane. For certain applications, there is difficulty in using this L because the rate of shear $\dot{\gamma}$ in principle should be infinity as the shear is limited to a single plane. This is the case, for example, in modeling of strain hardening if strain rate sensitivity is to be taken into account.[27] The evolution of the texture, however, is nearly independent of the strain rate.

In the flow line model, the following flow function was used for a better approximation of the material flow in the ECAE die:

$$\phi = (d - x)^n + (d - y)^n = (d - x_0)^n \qquad [2]$$

In this expression, d is the diameter of the die, x_0 defines the incoming (and outgoing) position of the flow line, and n is a parameter. This function is only valid in the working part of the die, *i.e.*, between the lines defined by $y = d$ and $x = d$. At these positions, the flow lines are perfectly parallel to the compression direction and the outgoing flow direction, respectively. The n parameter describes the possible shapes of the flow lines: for $n = 2$, the line is circular; for higher n values, it approximates the flow better within a nonrounded die. For $n \to \infty$, the flow line is constituted by simply two straight lines connected at the 45 deg symmetry plane of the die, as in the discontinuous shear model. The flow line function leads to the following velocity gradient:

Table III. Intensities as well as Rotation Angles from the Ideal Positions of the Measured and Simulated Texture Components for Material I

			Intensity Maximum (Times Random)					Rotation from Ideal Position in ϕ_1 (Deg, ±1 Deg)				
	Pass	Texture Index, T	A_{2E}	A_{1E}	C_E	$A_E/\overline{A_E}$	$B_E/\overline{B_E}$	A_{2E}	A_{1E}	C_E	$A_E/\overline{A_E}$	$B_E/\overline{B_E}$
Experiment	1	5.89	4	12	12	6	6	+6	−5	+1	0	−2
	2	7.62	4	16	4	6	12	+20	+6	+14	+9	+12
	3	4.80	3	12	2	2	8	+19	+2	+12	+8	+13
Flow line with self-consistent	1	6.10	4	16	16	3	6	+4	−4	+5	0	+3
	2	8.24	4	16	10	3	8	+17	+2	+9	+5	+7
	3	7.03	4	16	4	3	6	+17	+5	+9	+8	+10
Flow Line with Taylor	1	4.13	3	12	16	3	4	+4	0	0	0	+3
	2	5.07	0	20	12	4	4	—	+5	+6	+4	+2
	3	6.19	0	24	12	4	4	—	+4	+5	+6	+5
Simple shear with Taylor	1	3.74	0	12	16	2	6	—	−1	−2	0	0
	2	5.16	0	20	8	4	4	—	0	0	0	−1
	3	5.69	0	24	10	4	3	—	0	−3	−2	0
Simple shear with self-consistent	1	4.76	4	16	12	4	4	+2	−5	+2	−4	−2
	2	7.18	4	24	10	3	10	+3	−6	+5	−1	0
	3	6.62	6	10	4	6	12	+4	−5	+5	−2	0

Table IV. Intensities as well as Rotation Angles from the Ideal Positions of the Measured and Simulated Texture Components for Material II

			Intensity Maximum (Times Random)					Rotation from Ideal Position in ϕ_1 (Deg, ±1 Deg)				
	Pass	Texture Index, T	A_{2E}	A_{1E}	C_E	$A_E/\overline{A_E}$	$B_E/\overline{B_E}$	A_{2E}	A_{1E}	C_E	$A_E/\overline{A_E}$	$B_E/\overline{B_E}$
Experiment	1	6.27	0	4	24	2	3	—	−5	+4	0	+5
	2	5.03	2	20	3	2	6	+13	0	+8	+7	+8
	3	4.03	8	10	0	3	8	+11	−6	—	+4	+5
Flow Line with Self-Consistent	1	13.13	2	10	24	3	3	+4	−5	+1	−2	+1
	2	15.09	3	24	10	3	4	+18	+2	+10	+8	+11
	3	5.85	8	12	4	8	8	+15	+5	+9	+8	+9
Flow Line with Taylor	1	3.72	2	8	20	2	3	+5	0	0	+1	+4
	2	4.81	4	12	10	3	8	+11	+3	+4	+7	+10
	3	5.06	0	20	12	3	3	—	+4	+4	+8	+8
Simple shear with Taylor	1	4.06	0	8	12	3	3	—	0	−2	0	0
	2	4.68	0	12	10	4	10	—	−2	−2	0	+2
	3	4.39	0	16	12	4	2	—	−2	−2	0	0
Simple shear with Self-Consistent	1	10.49	2	8	24	3	3	0	−9	0	−5	−5
	2	13.17	4	24	8	2	6	+5	−5	+5	0	0
	3	6.07	12	8	4	8	10	+2	−6	+5	−2	0

Table V. Intensities as well as Rotation Angles from the Ideal Positions of the Measured Texture Components for Material III

			Intensity Maximum (Times Random)					Rotation from Ideal Position in ϕ_1 (Deg, ±1 Deg)				
	Pass	Texture Index, T	A_{2E}	A_{1E}	C_E	$A_E/\overline{A_E}$	$B_E/\overline{B_E}$	A_{2E}	A_{1E}	C_E	$A_E/\overline{A_E}$	$B_E/\overline{B_E}$
Experiment	1	5.58	2	16	2	1/1	4/12	+13	−4	+9	+1/+6	+6/+4
	2	3.86	0	3	3	6/0	6/6	—	−6	+7	0/−	+1/0
	3	5.81	3	3	2	2/4	12/8	+6	−7	+4	0/0	+2/−1

$$L = \begin{pmatrix} -v_0(1-n)(d-x)^{n-1}(d-y)^{n-1}(d-x_0)^{1-2n} & v_0(1-n)(d-x)^{n}(d-y)^{n-2}(d-x_0)^{1-2n} & 0 \\ -v_0(1-n)(d-y)^{n}(d-x)^{n-2}(d-x_0)^{1-2n} & v_0(1-n)(d-x)^{n-1}(d-y)^{n-1}(d-x_0)^{1-2n} & 0 \\ 0 & 0 & 0 \end{pmatrix} \quad [3]$$

As can be seen, this L is completely determined by experimental parameters, except for n, the parameter describing the shape of the line. Because it is quite difficult to measure the exact shape of the flow line (nevertheless, some results are published in Reference 8), the n parameter was determined with the help of texture simulations using comparisons with the experimental texture ("inverse method"). This is possible because the development of the crystallographic texture depends on the imposed strain path. The main effect of the n parameter is a small shift of the texture around the TD axis. This technique permitted identification of the strain mode in the ECAE die. Some finite-element simulations were also used to calibrate the n value in the first pass.[17] Reasonable values for n lie between 4 and 12. In the present simulations, it was found that for materials I and II, the best n value is 9 in the first pass and 4 in passes 2 and 3. Simulation results are not presented for material III (refer to the reasons given in Section V).

The ECAE simulations involve large strains, even in one pass (shear strain of about 2.0). Therefore, it cannot be expected that polycrystal models are able to simulate texture development continuously for a large number of passes. Actually, existing polycrystal models begin to fail after a shear strain of about 5. For this reason, simulations were also carried out using the so-called "texture-correction technique" introduced and employed in Reference 17. Under these circumstances and due to the availability of texture data after each pass, it is better to use the experimental texture as an input, not only in the first pass, but also in subsequent passes. In this way, the errors coming from the modeling do not get accumulated but are corrected at least after each increment of shear strain about 2.0. Actually, even if a texture is very well simulated in one pass, the deviations between the simulated and experimental textures can increase considerably in the later passes if the output texture after a simulated pass is used as an input in the next one. The progressive failing of the texture simulations also comes from experimental effects that are not completely taken into account in the modeling. For example, in the ECAE, the grain refinement process leads to increasing misorientations between subgrains. This effect is difficult to model; nevertheless, some efforts have been done in this direction (refer to the texture model of Beyerlin *et al.*,[28] and the more recent misorientation model of Estrin *et al.*)[29] The grain refinement process is not modeled in this work; we believe that the use of the preceding texture-correction technique accounts for it, at least partially, which modifies the input texture during each pass. Most of the simulation results presented here are obtained with the so-called texture-correction technique. For comparison purposes, simulations were also conducted with the continuous technique, that is, using the simulated textures in subsequent passes. These results are presented in Table VI. The subsequent discussions concern the results obtained by the texture-correction technique, unless otherwise stated.

In order to quantify the deviations between simulated and experimental ODFs, the texture index of the difference ODF (will be called DODF hereafter) will be employed in this work in the same way as it was used in References 14 and 15. The texture index was introduced by Bunge[24] by the following definition:

$$T = \int_{\text{Euler space}} [f(g)]^2 \, dg \quad [4]$$

where g means the orientation, identified by the Euler angles ϕ_1, ϕ, and ϕ_2; and $f(g)$ is the ODF intensity at g. The value of T increases as texture sharpens. When the difference between the simulated $f_{\text{sim}}(g)$ and experimental ODF $f_{\text{exp}}(g)$ is used in place of $f(g)$ in Eq. [4], T describes the strength of the *deviation* between the two textures:

$$T_{\text{DODF}} = \int_{\text{Euler space}} [f_{\text{sim}}(g) - f_{\text{exp}}(g)]^2 \, dg \quad [5]$$

Obviously, the smaller the T_{DODF} value, the better is the simulation. For the purposes of comparing the quality of simulation for different materials and for different modeling conditions, the T_{DODF} quantity can be normalized by the texture index of the simulated or the experimental texture. In this work, the normalization is done with respect to the *experimental* texture leading to the following parameter of the "texture-simulation quality":

Table VI. Texture Strength (T), Texture Index of the Difference ODF (T_{DODF}) and the Normalized Texture Index of the Difference ODF ($\hat{T}_{\text{DODF}}$), Obtained by *Continuous* Simulations of the Passes for Materials I and II

		Flow Line with Self-Consistent			Flow Line with Taylor			Simple Shear with Taylor			Simple Shear with Self-Consistent		
	Pass	1	2	3	1	2	3	1	2	3	1	2	3
Material I	T	6.10	11.39	11.24	4.13	10.93	9.99	3.74	6.80	7.77	4.76	10.74	14.46
	T_{DODF}	1.79	18.50	14.79	1.95	12.67	7.51	1.80	11.27	8.89	1.30	15.62	14.47
	$\hat{T}_{\text{DODF}}$	0.30	2.43	3.08	0.33	1.66	1.56	0.31	1.48	1.85	0.22	2.05	3.01
Material II	T	13.13	53.46	30.50	3.72	7.12	13.11	4.06	7.11	7.71	10.49	35.27	28.76
	T_{DODF}	4.26	40.34	25.67	2.48	4.79	12.05	3.47	6.93	8.98	5.56	23.51	26.42
	$\hat{T}_{\text{DODF}}$	0.68	8.02	6.37	0.57	0.95	2.99	0.69	1.38	2.23	1.13	4.67	6.56

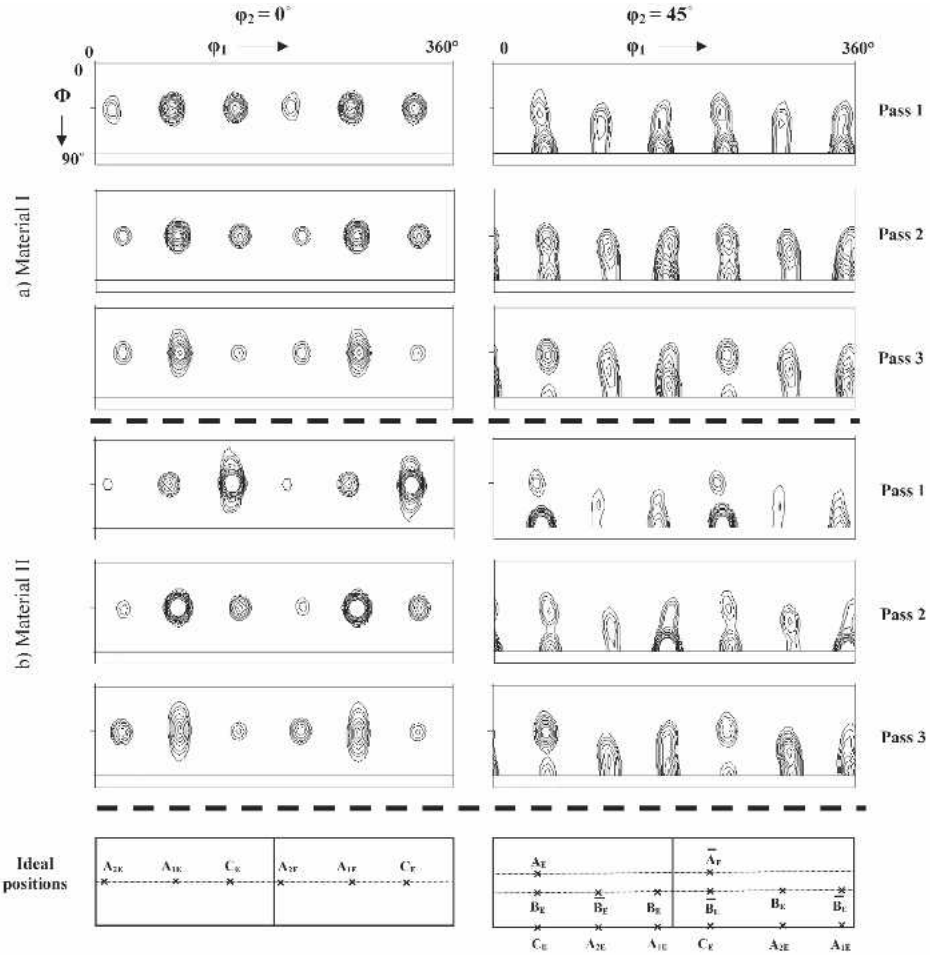

Fig. 7—ϕ_2 = 0 deg and ϕ_2 = 45 deg sections of the simulated ODF for (*a*) material I and (*b*) material II. Simulations carried out using the flow line model with self-consistent formulation.

$$\hat{T}_{\mathrm{DODF}} = \frac{\int_{\text{Euler space}} \left[f_{\mathrm{sim}}(g) - f_{\mathrm{exp}}(g) \right]^2 dg}{\int_{\text{Euler space}} \left[f_{\mathrm{exp}}(g) \right]^2 dg} \qquad [6]$$

Simulations have been carried out using the Taylor and self-consistent models for both the discontinuous and flow line cases. In order to save space, the resulting ODFs are presented only for the flow line model under self-consistent conditions and using the texture-correction technique (Figure 7). For the other cases, the results obtained for the main components are displayed in Tables III and IV. The texture-simulation-quality index ($\hat{T}_{\mathrm{DODF}}$) is plotted in Figure 8.

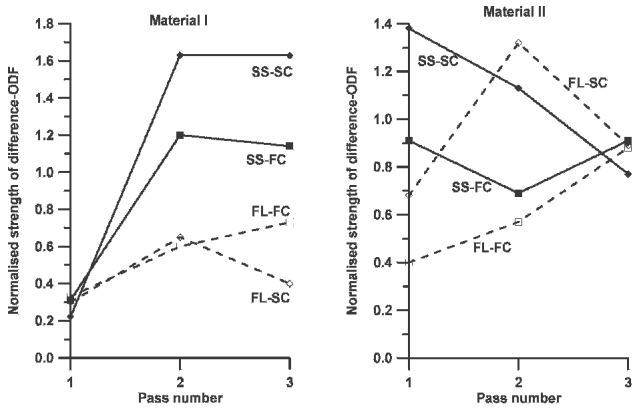

Fig. 8—The normalized texture index of the different ODFs between simulations and experience for materials I and II.

B. *Discontinuous Shear Approach with Taylor Polycrystal Model*

By comparing the textures predicted by the discontinuous shear approach using Taylor formulation to the experimental textures, one could say that in the first and second passes, the intensities of the components match reasonably well the experimental texture for material I (Table III). The main difference is that the A_{2E} component is completely absent in the simulation after one pass. In the third pass, the A_{1E} component is too strong compared to the experiments. Concerning the predicted positions of texture components, one can see in Table III that they do not change significantly with the pass number in the Taylor formulation using the discontinuous shear approach, which is in contrast to the experimental observations. These trends are almost repeated for material II (Table IV). The additional feature for this material is the prediction of strong maxima at rotated cube positions (not shown here because of space

limitations), which are although present, substantially weaker in the experimental texture (Figure 6(b)).

C. *Discontinuous Shear Approach with Self-Consistent Polycrystal Model*

The results obtained with the SC formulation are better than those of the Taylor formulation. The major improvement is that the A_{2E} component is now predicted for both materials (Tables III and IV).

Previous simulations in other works[22,30] have also used the discontinuous shear approach employing the SC formulation and reported good agreement with experiments. However, their analysis is qualitative, based on pole figures, not on ODFs. When the textures are presented in pole figures, they seem to match better the experiments, however, just in appearance.

D. *Textures Predicted by the Flow Line Model*

For material I, the intensities and the positions of texture components obtained by the Taylor model are quite well reproduced in the first pass. The comparison in the second pass is less satisfactory because the A_{2E} component is absent in the simulation and the positions of $B_E/\overline{B}_E$ and C_E components deviate about 10 deg from the experimental ones. The situation is even worse in the third pass where the A_{1E} component becomes excessively strong.

The results obtained with the self-consistent model are displayed in Figure 7. By comparing the intensities of the components between experiments and simulations in Table III for material I, one can say that the self-consistent model performs the best with respect to the other modeling conditions. A major improvement of the textures for the self-consistent case is a much better prediction of the positions of the ideal components. These positions are reproduced within 4 deg in all passes (an exception is the $B_E/\overline{B}_E$ where the differences are somewhat larger). According to the data in Table IV and Figure 7 for material II, it is again the self-consistent model, which seems to perform the best. However, the predicted texture index is very high with respect to the experiments (Table IV).

V. DISCUSSION

The results presented in Section IV concern textures with similar components for materials with different purity levels for different initial textures. It has been shown that the intensities and location of the texture components depend on material characteristics. In this section, an attempt has been made to understand the texture evolution with the help of the experimental and simulation results. First, the quality of the texture simulations will be examined. This part only concerns materials I and II. For material III, simulation results are not presented. The reason for this is the extreme dependence of the textures on the initial one. This dependence is well demonstrated by the texture differences between materials I and II shown in Section III. For material III, however, the initial texture is not known because of the very large grain size of the cast material. Actually, the grain size is comparable to the sample width, which means that for this material, each sample has a very different initial texture (same sample could not be used repeatedly after each pass, because its texture had to be measured). The very high texture index of the initial texture (more than 100 (Table II)) is the consequence (and an indicator) of the very large grain size. Nevertheless, there are some interesting features worth discussing in the textures of material III. In spite of the fact that the textures shown in Figures 4 and 6 for this material for each pass are the result of *different* initial textures, they show some interesting *trends*. There is a progressive weakening of the A_{1E} component and the progressing formation of the $B_E/\overline{B}_E$. Such trends would not be expected if the initial texture would be a decisive factor of the texture development. We will come back to this point in more detail in the subsequent discussion.

A. *Texture Simulation Quality*

The details of the differences between simulated and experimental textures can be analyzed in terms of relative and absolute intensities of the texture components as well as by the deviations concerning their exact positions in Euler space. For this purpose, Tables III and IV are very useful. It is necessary, however, to have more general ideas about the success of the different models employed in the present article. This is why the texture index of the *difference* ODF was calculated according to Eq. [6] and presented in Figure 8. This figure presents the results for all four simulation approaches employed in this work according to the following notation: FL: flow line approach; SS: simple shear approach (also called "discontinuous shear" in this work and in Reference 17); SC: self-consistent model; and FC: full constraints (Taylor) polycrystal model.

As can be seen in Figure 8, the normalized texture index of the difference ODF is very low for material I for all four models in the first pass. Although details of the simulated textures seem to be best reproduced by the FL-SC model, other models perform also very well in terms of general texture agreement. The main reason for this is that in the first pass, the FL approach is used with a high n parameter for the flow line meaning that the flow lines approach quite well the simple shear conditions in the first pass. In passes 2 and 3, however, it is only the FL-SC model that gives the best agreement with the experiments (exception is the FL-FC approach for pass 2). In these passes, the n value is low, only 4, which means that deviations from simple shear conditions are important in passes 2 and 3. Note that the $\hat{T}_{DODF}$ values in Figure 8 are in the same range as those reported for copper by Li *et al.*,[14] who employed *finite element* simulations for a rounded die.

For material II, the situation is different. Namely, in the first pass, the quality of the simulated textures is significantly smaller (meaning higher $\hat{T}_{DODF}$ values) than in material I. For this material, it is the FL-FC model that is the best in the first pass. This difference can be interpreted in the following way. Material II has a very strong initial texture. The texture index is 11.02 for the starting texture (which is only 2.88 for material I (Table II)). The texture initially is a strong cube type, meaning that there is not much difference between the orientations of individual grains. Consequently, there cannot be significant differences either in their behavior, namely, in their deformation. That is, nearly Taylor conditions must apply. The self-consistent model permits larger differences in the deformations of individual grains that cannot be the case in this material. At pass number 3, all models seem to perform equally, possibly for the reason that the ECAE deformation texture becomes very different from the initial cube texture. The FL-SC model leads to unusually strong deformation textures in the first two

passes (texture index in Table IV), which is also a reason for the relatively high $\hat{T}_{DODF}$ values for this case.

The preceding discussion is based on simulated textures obtained with the help of the texture-correction technique. When the simulation is continuous through all three passes, the predicted textures are in lesser agreements with experiments. Detailed simulation results are not shown here for this case; only the texture-quality index was calculated to indicate the main trends. They are presented in Table VI. The $\hat{T}_{DODF}$ values in this table clearly demonstrate that the deviations between simulations and experiments are much more significant compared to the results obtained with the help of the texture-correction technique.

B. *Comparisons with Simple Shear*

The first important observation that could be made out of these studies is that a typical shear-type texture forms after the first pass itself, with components that depend on the initial texture. The main difference appears in terms of relative intensities of the components, and further variations in their intensities. Results of this investigation further reinforce the concepts proposed in earlier works[8,20,17,30,31] that texture development during ECAE is similar to that under torsion, however, with important differences. For high stacking fault energy fcc metals, such as aluminum, torsion textures are typically found to consist of a partial <110> fiber and a less strong partial {111} fiber,[25] indicating a strong tendency for the slip direction to align with the shear direction. In ECAE of aluminum alloy[8] as well as copper,[10,11,12] the ideal C_E and B_E components are normally positions of higher orientation density on the partial <110> fiber. Recently, we reported the ECAE texture of silver to consist mainly of the $B_E/\overline{B}_E$ components.[20] The study of *torsion* texture of Ni-Co alloys by Hughes *et al.*[32] using ODFs has identified the major components for a high to medium Stacking Fault Energy (SFE) material (Ni or Ni-30Co) as A, B, C, and A_1* for intermediate deformation and C for larger deformations, whereas for a low SFE alloy (Ni-60Co), the components are A, B, and A_1*, which do not change with deformation for medium to high strains. In the current study, texture of copper, which is a medium stacking fault energy material, reveals the occurrence of the corresponding ECAE texture components in the first pass for both the materials I and II. However, their intensities do not remain constant, and a gradual variation is noticed with further ECAE deformation. Rotation from respective ideal positions was noticed in all the cases by Hughes *et al.*,[32] however, to a lesser extent and occurring in the opposite direction with respect to ECAE textures.

C. *Deviations from Ideal Positions*

The other important feature of the ECAE textures of copper, which are common to the textures of both materials I and II, are the rotations of ideal components from their symmetry position. The texture components for material I appear within 6 deg of the ideal positions in the first pass but deviate from them up to 20 deg in subsequent passes. The tilts from the exact ideal positions for simple shear were examined by Tóth *et al.*, in References 33 through 35 and were explained with the help of the convergent/divergent nature of the rotation field in Euler space. In those works the shear direction was positive, while in ECAE the shear is negative in the reference system used in this work. Thus, the tilts of the components should be opposite. (Only the first pass ECAE textures can be compared to the textures measured in simple shear.) One can see, however, that by comparing the values obtained for the first pass in materials I and II in the present work to the values published in Reference 35 (by taking into account the opposite shear directions), they do not match each other. Actually, they are in opposite sense. The explanation is that the ideal components of ECAE textures are not exactly located at positions where they are expected to be from simple shear. The deviations in the first pass are on the order of 4 to 7 deg in orientation space. The flow line model is able to account for these differences, as can be seen from the simulation results presented in Tables III and IV. In the first pass, the flow line shapes were modeled with an n parameter of 9. Thus, one can conclude that this value leads to a significantly different strain path with respect to exact simple shear. The situation is even more problematic starting from the second pass. The very large rotations, going up to 20 deg, mean that the strain path deviates even more from ideal simple shear. The flow line model is able to account for these differences by simply employing lower n values (n was lowered from 9 to 4 from the second pass in the simulations). As can be seen in Tables III and IV, the tilts of texture components are quite reasonably reproduced by the flow line approach in the second and third passes as well, when the SC model is employed. It is probable that the combined effect of hardening and friction is responsible for the change of strain path (which is reflected by the n value) between pass one and later passes. This question will be examined in future works. It is also quite probable that the change of straining direction between passes (rotation of the sample by 90 deg) has an important role in the tilts of the ideal components.

D. *Behavior of Ideal Components*

In all three materials (only exception is material I, for pass 3), there is a strengthening of the $B_E/\overline{B}_E$ components with the pass number. This phenomenon can also be explained on the basis of the flow field. Actually, after each pass, the sample has to be turned by -90 deg around the TD (Z-direction in Figure 1) for reinserting it into the die for the next pass. This corresponds to an overall shift of the texture by 90 deg in the *decreasing* ϕ_1 direction in orientation space. This means that the $B_E/\overline{B}_E$ components of the first pass will now be on the *left side* of the new ideal $B_E/\overline{B}_E$ positions by 30 deg in the ϕ_1 coordinate. Therefore, in the subsequent pass, they will further strengthen because of the *convergent* nature of the rotation field on the left side of the ideal orientations. It is to be noted that the $B_E/\overline{B}_E$ components are symmetrically located at every 60 deg in orientation space (key figure in Figure 6); thus, their strengthening is due to their symmetry.

The major difference in the textures of materials I and II is the evolution and strengthening of the A_{1E} component. As the textures are well reproduced by the modeling, one cannot say that the differences in the texture evolution are due to the differences in purity or SFE. It is clear that it is simply the strong differences in the *initial* textures that are responsible for the differences in their subsequent evolution.

E. *Hardness*

Brinell hardness measurements have been carried out in order to examine the result of the hardening process after ECAE (Figure 9). In its initial state, material I is the softest, probably because this is the purest. At the same time, this material presents the largest amount of strengthening after the first pass with maximum hardness. The hardness just slightly increases in the second pass, while it *decreases* after the third. There is no such decrease for materials II and III after the third pass. The high hardness of material I after the first pass could be attributed to its texture. Namely, the main texture component in this material is a very strong C_E, which has the highest Taylor factor among all ideal shear components.[36] The decrease of hardness after the third pass is probably due to some dynamic restoration process (recovery or partial recrystallization), as discussed in Section F.

F. *Microstructure*

The microstructure of material I after three passes, as recorded using a scanning electron microscope operated in backscattered detection mode, is shown in Figure 10. The few white grains seen in the microstructure support the existence of a dynamic restoration process in this pure material. This effect can be responsible for the decrease of hardness after pass 3 in material I. The texture evolution may be more sensitive to composition for material III, due to the influence of impurity elements on stacking fault energy (SFE) (Be 0.011 pct, Co 0.044 pct, Sn 0.026 pct, Pb 0.05 pct, and other elements such as Se, Te in minor quantities). It should be mentioned here that simulation work incorporating twinning, which is quite frequently observed in low stacking fault energy materials,[37] leads to a shear texture dominated by the $B/\overline{B}$ components. In a more recent work, Tóth *et al.*[38] have shown that not only the $B/\overline{B}$ components are strong but the A_{1E} component disappears in ECAE of silver (a low stacking fault energy material) because of its ease for deformation twinning. The same trend can be seen in the texture evolution of material III in Figure 6. Figure 11 shows a TEM micrograph of three-pass deformed material III. As can be seen, the microstructural feature indicates the presence of twins. The occurrence of twinning together with the strong $B_E/\overline{B}_E$ component promotes the idea of a strong relation between SFE–twinning–evolution of texture components.

A third factor that may be responsible is the effect of grain size. It is established that the acquisition of final texture is delayed during rolling of coarse-grained materials.[39] This is closely related to the influence of grain size on deformation behavior, or more precisely on deformation patterns.[40] This subject has been discussed more recently in terms of polycrystal models.[41,42] Material III of the present investigation represents a similar situation, however, having been subjected to a different type of deformation process.

The last point in the microstructural observation in material III is the presence of impurity particles in form of oxides. An approximate quantitative estimate of the initial microstructure indicates that their volume fraction is about 1 pct. It can be seen (Figure 12) that these particles are able to influence the deformation pattern and the microstructure quite significantly. Also, the nucleation of cracks is quite visible along these particles. At this moment, it is difficult to comment on their role on texture evolution until a systematic study is carried out on texture evolution regarding two-phase alloys or composites. Another interesting observation made on this material is worth mentioning. This is

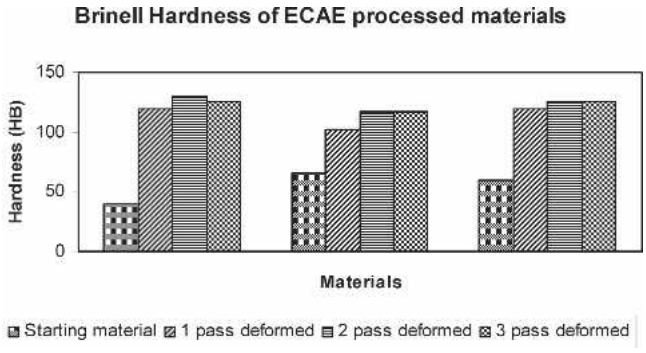

Fig. 9—Results of Brinell hardness measurements on the starting and the ECAE-deformed materials.

Fig. 10—Microstructure of material I after three passes of ECAE, as recorded using the scanning electron microscope (SEM) operated in backscattered detection mode.

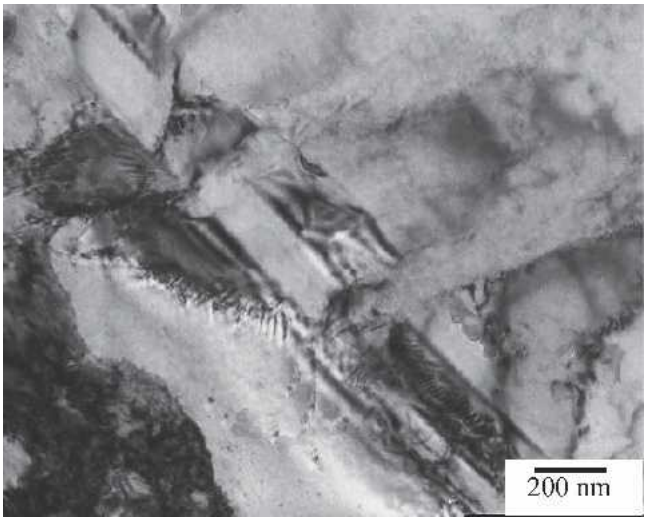

Fig. 11—TEM micrograph of three-pass ECAE-deformed material III.

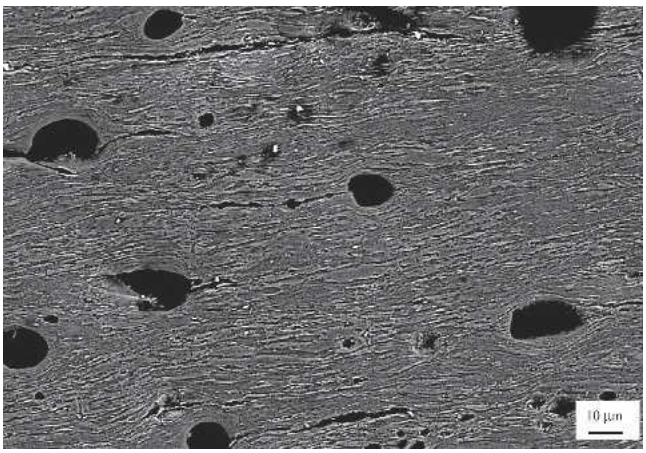

Fig. 12—SEM micrograph of three-pass ECAE-deformed material III.

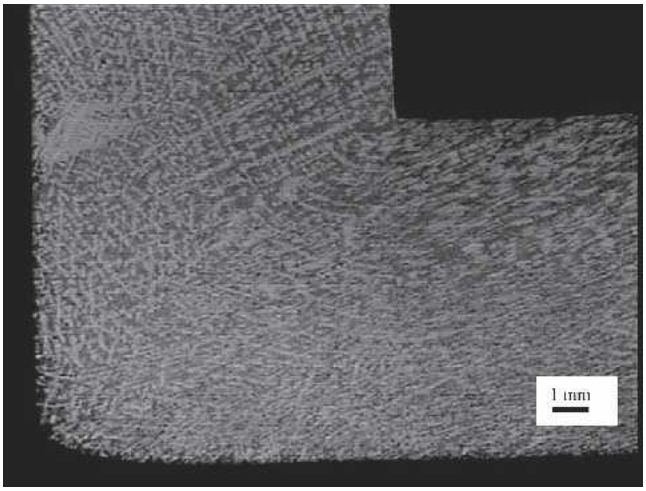

Fig. 13—Optical macrograph of material III deformed halfway through.

related to the bending of dendrites in material III in ECAE. Figure 13 shows the low-magnification optical macrostructure recorded from the one-pass deformed material. In order to depict the features introduced due to ECAE deformation, only half of the material was passed through the die. The rest was kept undeformed and the sample was taken out from the die. The dendrites reveal the large grain structure before the plastic strain zone as well as the extent of the latter where the dendrites are curved.

VI. CONCLUSIONS

In the present work, experimental results are presented for textures and microstructures of polycrystalline copper for different starting conditions in terms of initial textures, purity, and grain size. With the help of polycrystal simulations, the texture development was modeled with different models using the so-called "texture-correction" technique. The main observations of the experiments and the analysis of the results obtained in the simulations can be summarized in the following main conclusions.

1. A strong texture forms in copper as a result of ECAE (route A) deformation, which strengthens further in the second pass, however, weakens slightly in the third pass. The texture mainly consists of strong $B_E/\overline{B}_E$, A_{1E} components and weaker C_E and A_{2E} components, each rotated significantly by different amounts from their expected ideal position. With an increase in the amount of deformation, all three materials show an increase of these shifts.
2. In the wrought materials, the A_{1E} components strengthen from the first to the second pass and the A_{2E} and C_E components weaken in subsequent passes. In the cast material, the A_{1E} component, which is predominantly strong in the first pass, weakens in subsequent passes, while the A_{2E} and C_E components remain weak from the beginning to the last pass.
3. The evolution of an overall shear-type texture in ECAE-deformed copper is found to be dependent of the material variables. The finer details of the texture including the relative intensities and volume fraction of individual texture components are quite sensitive to the starting microstructure and impurity content of the starting material.
4. It is possible to predict texture evolution using simple shear as well as flow line models. The latter gives better results, especially for the shifts of the texture components from their positions of symmetry.

ACKNOWLEDGMENTS

The authors gratefully acknowledge the help rendered by J.-P. Mathieu and P. Moll during the ECAE experiment. One of the authors (SS) acknowledges the postdoctoral fellowship accorded by the Ministry of Research, Government of France. He is also grateful to the Defence Research and Development Organisation, Ministry of Defence, Government of India, for granting leave to carry out this work.

REFERENCES

1. V.M. Segal: *Mater. Sci. Eng. A*, 1995, vol. A97, pp. 157-64.
2. R.Z. Valiev: *Mater. Sci. Eng. A*, 1997, vols. A234–A236, pp. 59-66.
3. V.M. Segal: *Mater. Sci. Eng. A*, 1999, vol. A271, pp. 322-33.
4. I.V. Alexandrov, Y.T. Zhu, T.C. Lowe, R.K. Islamgaliev, and R.Z. Valiev: *Metall. Mater. Trans. A*, 1998, vol. 29A, pp. 1047-58.
5. Y.T. Zhu and T.C. Lowe: *Mater. Sci. Eng. A*, 2000, vol. A291, pp. 46-53.
6. C. Pithan, T. Hashimoto, M. Kawazoe, J. Nagahora, and K. Higashi: *Mater. Sci. Eng. A*, 2000, vol. A280, pp. 62-68.
7. S.R. Terhune, D.L. Swisher, K. Oh-Ishi, Z. Horita, T.G. Langdon, and T.R. McNelley: *Metall. Mater. Trans. A*, 2002, vol. 33A, pp. 2173-84.
8. A. Gholinia, P. Bate, and P.B. Prangnell: *Acta Mater.*, 2002, vol. 50, pp. 2121-36.
9. V.M. Segal: *Mater. Sci. Eng. A*, 2002, vol. 338, pp. 331-44.
10. W.H.C. Huang, L. Chang, P.W. Hao, and C.P. Chang: *Mater. Sci. Eng. A*, 2001, vol. A307, pp. 113-18.
11. I. Kopacz, M. Zehetbauer, L.S. Tóth, I.V. Alexandrov, and B. Ortner: *Proc. 22nd Risø Symp. on Science of Nanocrystalline and Metastable Alloys, Structure Properties and Modelling*, Dinesen *et al.*, ed., Risø National Laboratory, Roskilde, Denmark, 2001, pp. 295-300.
12. L.S. Tóth, M. Zehetbauer, I. Kopacz, and I.V. Alexandrov: *Proc. THERMEC' 2000*, Las Vegas, NV, Dec. 4–8, 2000, Elsevier, *J. Mat. Proc. Techn.*, on CD only: ISBN 0080440266.
13. S. Ferrasse, V.M. Segal, S.R. Kalidindi, and F. Alford: *Mater. Sci. Eng. A*, 2004, vol. 368, pp. 28-40.
14. S. Li, I.J. Beyerlin, C.T. Necker, D.J. Alexander, and M. Bourke: *Acta Mater.*, 2004, vol. 52, pp. 4859-75.

15. S. Li, I.J. Beyerlin, D.J. Alexander, and S.C. Vogel: *Acta Mater.*, 2005, vol. 53, pp. 2111-25.
16. M. Haouaoui, K.T. Hartwig, and E.A. Payzant: *Acta Mater.*, 2005, vol. 53, pp. 801-10.
17. L.S. Tóth, R. Arruffat-Massion, L. Germain, S.C. Baik, and S. Suwas: *Acta Mater.*, 2004, vol. 52, pp. 1885-98.
18. S.C. Baik, Y. Estrin, H.S. Kim, and R.J. Helmig: *Mater. Sci. Eng., A*, 2003, vol. 351, pp. 86-97.
19. W. Skrotzki, R. Tamm, R. Klemm, E. Thiele, C. Holste, and H. Baum: *Mater. Sci. Forum*, 2002, vols. 408–412, pp. 667-72.
20. S. Suwas, L.S. Tóth, J.-J. Fundenburger, A. Eberhardt, and W. Skrotzki: *Scripta Mater.*, 2003, vol. 49, pp. 1203-08.
21. M.A. Gibbs, K.T. Hartwig, L.R. Cornwell, R.E. Goforth, and E.A. Payzant: *Scripta Mater.*, 1998, vol. 39, pp. 1699-1704.
22. S.R. Agnew: *Proc. 12th Int. Conf. on Texture of Materials (ICOTOM-12)*, J.A. Szpunar, ed., NRC Research Press, Ottawa, 1999, pp. 575-80.
23. P. Van Houtte: ODF MTM–FHM Software, version 2000.
24. H.J. Bunge: *Texture Analysis in Materials Science*, Butterworth and Co., London, 1982.
25. F. Montheillet, M. Cohen, and J.J. Jonas: *Acta Metall.*, 1984, vol. 32, pp. 2077-89.
26. A. Molinari and L.S. Tóth: *Acta Metall. Mater.*, 1994, vol. 42, pp. 2453-53.
27. L.S. Tóth, A. Molinari, and Y. Estrin: *J. Eng. Mater. Technol.*, 2002, vol. 124, pp. 71-77.
28. I.J. Beyerlein, R.A. Lebensohn, and C.N. Tome: *Mater. Sci. Eng., A*, 2003, vol. 345, pp. 122-38.
29. Y. Estrin, L.S. Tóth, Y. Brechet, and H.S. Kim: *NanoSPD3 Conf.*, Fukuoka, Japan, Sept. 2005, in press.
30. S.R. Agnew, U.F. Kocks, K.T. Hartwig, and J.R. Weertman: *Proc. 19th Riso. Int. Symp. on Materials Science*, Roskilde, Denmark, 1998, pp. 201-06.
31. L.S. Tóth: *Adv. Eng. Mater.*, 2003, vol. 5, pp. 308-16.
32. D.H. Hughes, R.A. Lebenson, H.-R. Wenk, and A. Kumar: *Proc. R. Soc. London A*, 2000, vol. 456, pp. 921-53.
33. L.S. Tóth, K.W. Neale, and J.J. Jonas: *Acta Metall.*, 1989, vol. 37, pp. 2197-210.
34. L.S. Tóth, P. Gilormini, and J.J. Jonas: *Acta Metall.*, 1988, vol. 36, pp. 3077-91.
35. L.S. Tóth, J.J. Jonas, D. Daniel, and J.A. Bailey: *Text. Microstr.*, 1992, vol. 19, pp. 245-62.
36. J.J. Jonas and L.S. Tóth: *Scripta Metall. Mater*, 1992, vol. 27, pp. 1575-80.
37. P. Van Houtte: *Acta Metall.*, 1978, vol. 26, pp. 591-604.
38. L.S. Toth, I. Beyerlin, C.N. Tomé, and S. Suwas: unpublished research, 2005.
39. T. Leffers, D. Juul Jensen, and N. Hansen: *Proc. 8th Int. Conf. on Texture of Materials (ICOTOM-8)*, Santa Fe, NM, 1988, J.S. Kallend and G. Gottstein, eds., TMS, Warrendale, PA, 1987, pp. 449-54.
40. T. Öztürk, J.S. Kallend, and G.J. Davies: *Proc. 6th Int. Conf. on Texture of Materials (ICOTOM-6)*, S. Nagashima, ed., The Iron and Steel Institute of Japan, Tokyo, 1982, pp. 507-15.
41. H. Conrad: *Mater. Sci. Eng. A*, 2003, vol. 241, pp. 216-28.
42. A.J. Beaudoin, A. Acharya, S.R. Chen, D.A. Korzekwa, and M.G. Stout: *Acta Mater.*, 2000, vol. 48, pp. 3409-23.